Thermal Modulation of Defect Density and Lattice Hydration in Microwave-Hydrothermal Vanadium Pentoxide Cathodes for Aqueous Zinc-Ion Batteries

Boramith Phonly

A thesis submitted
in partial fulfillment of the
requirements for the degree of

Master of Science

University of Washington

2026

Committee:

Guozhong Cao

Bruce Hinds

Program Authorized to Offer Degree:

Materials Science and Engineering

University of Washington

Abstract

Thermal Modulation of Defect Density and Lattice Hydration in Microwave-Hydrothermal Vanadium Pentoxide Cathodes for Aqueous Zinc-Ion Batteries

Boramith Phonly

Co-chairs of the Supervisory Committee:
Guozhong Cao
Department of Materials Science and Engineering

Bruce Hinds
Department of Materials Science and Engineering

Practical deployment of aqueous zinc-ion batteries (AZIB) is constrained by sluggish Zn^{2+} transport and cathode structural degradation. Microwave-hydrothermal (MWHT) synthesis leverages dielectric volumetric heating to accelerate nucleation and promote homogeneous crystal growth, yet how synthesis temperature governs structural evolution in $V_2O_5 \cdot nH_2O$ cathodes has not been systematically established. This study investigates how a modest 20 °C thermal increment governs the crystalline ordering, defect density, and charge storage kinetics within the hydrated phase framework. V_2O_5 synthesized at 130 °C for 60 minutes yields a disordered, strongly hydrated phase characterized by crumpled nanosheets and a high V^{4+} defect concentration ($V^{5+}/V^{4+} = 6.5$). Increasing the synthesis temperature to 150 °C drives interlayer reorganization and crystallite ripening within the hydrated $V_2O_5 \cdot nH_2O$ framework, yielding well-faceted lamellae with improved long-range ordering and a reduced defect density ($V^{5+}/V^{4+} = 8.8$). The 130 °C cathode exhibits mixed kinetics with a diffusion-dominant contribution ($\bar{b} \approx 0.70$) and elevated charge-transfer resistance ($R_{ct} \approx 400\ \Omega$), whereas the 150 °C cathode shifts toward

pseudocapacitive-dominant charge storage ($\bar{b} \approx 0.85$) with 20% lower interfacial resistance (Rct ≈ 320 Ω). The 150 °C cathode delivers 330 mAh g^{-1} at 0.5 A g^{-1} and retains 64% capacity after 3000 cycles at 4 A g^{-1}, compared to 52.6% for the 130 °C sample. These findings demonstrate that MWHT synthesis temperature is a readily accessible parameter for simultaneously tuning crystalline ordering, defect density, and long-term cycling stability in hydrated vanadium oxide cathodes.

Table of Contents

1. Introduction

Aqueous zinc-ion batteries (AZIBs) represent a highly scalable energy storage architecture, utilizing water-based electrolytes to bypass the safety hazards of organic systems while exploiting the high theoretical specific capacity and natural abundance of metallic zinc. Despite these advantages, the practical deployment of AZIBs is constrained by structural and kinetic limitations of the cathode host [1]. To achieve stable long-term cycling, cathode materials must accommodate the mechanical strain of hydrated Zn^{2+} intercalation within the narrow electrochemical stability window of water (~1.23 V) without suffering from parasitic side reactions or structural dissolution.

Among vanadium-based host materials, vanadium pentoxide (V_2O_5) is a prominent cathode candidate for AZIBs due to its open lamellar framework and multielectron redox capability (V^{5+}/V^{3+}), which yields high theoretical specific capacities [2]. Charge-storage kinetics in V_2O_5 are strongly influenced by its hydration state. Intercalated structural water ($V_2O_5 \cdot nH_2O$) expands the interlayer d-spacing to 8–10 Å which provides electrostatic charge shielding that lowers the diffusion barrier for divalent Zn^{2+}. However, excessive hydration induces lattice swelling and structural instability during repeated cycling, particularly in poorly crystalline frameworks where disordered V–O bonding offers limited resistance to volume change [3]. Precise control over both hydration level and framework crystallinity is therefore essential for achieving durable, high-capacity V_2O_5 cathode performance.

Conventional hydrothermal synthesis relies on external conductive heating, producing non-uniform temperature gradients, prolonged reaction times of 12–24 hours, and batch-to-batch crystallinity variation. Microwave hydrothermal synthesis (MWHT) mitigates these limitations

through dielectric volumetric heating, which generates uniform thermal gradients, accelerates nucleation, and promotes homogeneous crystal growth [4]. Despite these kinetic advantages, the thermal parameters must be optimized against the thermodynamic stability of the aqueous solvent. While Jalil et al. identified the 140°C – 160°C window as the threshold for significant shifts in particle size and crystallinity, the upper bound of this regime approaches the safety limits of standard aqueous microwave reactors [5]. To maintain a safe vapor pressure margin of approximately 50 °C above the solvent boiling point, the upper synthesis temperature was capped at 150 °C. 130 °C and 150 °C were selected to capture the onset of structural evolution within this constrained thermal window. A fixed dwell time of 60 minutes was selected based on prior vanadium oxide synthesis under comparable microwave hydrothermal conditions [4].

In this research, V_2O_5 cathodes were synthesized via microwave-hydrothermal treatment at 130 °C and 150 °C for a fixed duration of 60 minutes. The structural, morphological, and chemical evolution of the host lattice was characterized using X-ray diffraction (XRD), scanning electron microscopy (SEM), Raman spectroscopy (RAMAN), and X-ray photoelectron spectroscopy (XPS). Concurrently, cyclic voltammetry (CV), galvanostatic charge–discharge (GCD), and electrochemical impedance spectroscopy (EIS) were employed to evaluate Zn^{2+} diffusion kinetics and charge storage mechanisms. Together, these analyses establish how a 20 °C thermal increment governs defect density, crystalline ordering, and charge-storage kinetics within the hydrated $V_2O_5 \cdot nH_2O$ framework. These findings establish MWHT synthesis temperature as a readily accessible design parameter for tuning defect density and structural ordering in vanadium-based AZIBs.

2. Methods

2.1 Materials and synthesis

The cathode material was synthesized via a microwave-assisted hydrothermal method using a Biotage Initiator reactor. V_2O_5 (2 mmol) and H_2O_2 (30 wt%, 2 mL) were dissolved in deionized water (50 mL) and magnetically stirred for 30 minutes. The precursor solution was transferred into a sealed microwave vial and heated to either 130° C or 150 °C for 60 min in fixed hold-time mode (absorption level: High; pressure limit <15 bar; stirring off). After cooling to room temperature, the resulting suspension was transferred into a beaker, covered with a Kimtech wipe, and rapidly frozen by immersion in a Teflon basket filled with liquid nitrogen. The frozen product was then freeze-dried at -52 °C under low vacuum for 4 days to preserve the open, porous microstructure, and further vacuum-dried at 120 °C for 2 hours to remove residual adsorbed water. Both samples were processed identically through all the post-synthesis steps to ensure that structural and electrochemical differences are attributed solely to synthesis temperature [6].

2.2 Material Characterization

Phase identification was carried out by powder X-ray diffraction (XRD) using a Bruker D8 Discover diffractometer equipped with an IμS 2-D XRD system. Morphology and microstructure were examined by field-emission scanning electron microscopy (FE-SEM, Apreo Variable Pressure SEM, Thermo Fisher Scientific). Elemental composition and distribution were analyzed by energy-dispersive X-ray spectroscopy (EDS) on the same instrument. Raman spectra were collected on a Renishaw confocal Raman microscope using a 785 nm laser excitation source. X-ray photoelectron spectroscopy (XPS) was conducted on a Kratos Axis Supra+ spectrometer

equipped with a monochromatized Al Kα source. Charge compensation was applied to correct for surface charging on the non-conducting oxide. Spectra were analyzed using Kratos ESCApe software with Shirley background subtraction, and all binding energies were calibrated to the C 1s C–C peak at 285.0 eV.

2.3 Electrochemical Measurement

Cathode electrodes were fabricated by dispersing the active material, conductive carbon black, and poly(vinylidene fluoride) (PVDF) binder in N-methyl-2-pyrrolidone (NMP) at a mass ratio of 7:2:1. The resulting slurry was cast onto titanium foil current collectors, dried at 60 °C, and subsequently vacuum-dried at 120 °C for 12 h. CR2032 coin cells were then assembled in ambient air, with zinc metal foil as the counter electrode, glass fiber as the separator, and 3 M zinc trifluoromethanesulfonate ($Zn(CF_3SO_3)_2$) aqueous solution as the electrolyte. All electrochemical measurements were conducted within a potential window of 0.2–1.6 V vs. Zn^{2+}/Zn. Galvanostatic charge–discharge (GCD) and cyclic voltammetry (CV) were performed on a Neware CT-4008 battery tester, while electrochemical impedance spectroscopy (EIS) was conducted on a Solartron SI-1287/1260 system [6].

3. Results and Discussion

3.1 Structural and Morphology

This section establishes the synthesis–structure relationships governing the two MWHT V_2O_5 cathodes through a suite of characterization techniques. Phase composition and long-range crystalline order are evaluated by XRD, while SEM and EDS resolve morphological architecture and bulk stoichiometry, respectively. Raman spectroscopy probes local V–O vibrational modes

and lattice disorder. XPS resolves surface vanadium oxidation states and defect density. These characterization data establish how a 20 °C thermal increment governs lattice hydration, crystalline ordering, and defect chemistry in the hydrated $V_2O_5 \cdot nH_2O$ framework.

3.1.1 Phase composition and crystal structure (XRD)

XRD patterns of both samples confirm phase identity within the hydrated $V_2O_5 \cdot nH_2O$ framework. The 130 °C sample exhibits an intense low-angle (001) reflection at $2\theta \approx 7°$, corresponding to an expanded interlayer d-spacing of ~11–13 Å, consistent with structural H_2O molecules occupying the [VO_5] interlayer galleries [3]. The higher-angle reflections are weak and broadened, indicating limited long-range periodic ordering. In AZIBs, interlayer structural water facilitates Zn^{2+} migration by charge-shielding the divalent ion and lowering the diffusion barrier. However, excessive hydration introduces lattice swelling and structural instability during repeated cycling [11].

At 150 °C, the low-angle (001) reflection is attenuated but remains detectable, indicating the sample retains its hydrated phase identity while the interlayer environment reorganizes. The (110), (600), (020), and (321) reflections sharpen considerably, confirming improved long-range crystalline ordering relative to the 130 °C sample [6]. Collectively, these diffraction features establish that 150 °C synthesis yields a better-ordered and less heavily hydrated $V_2O_5 \cdot nH_2O$ framework.

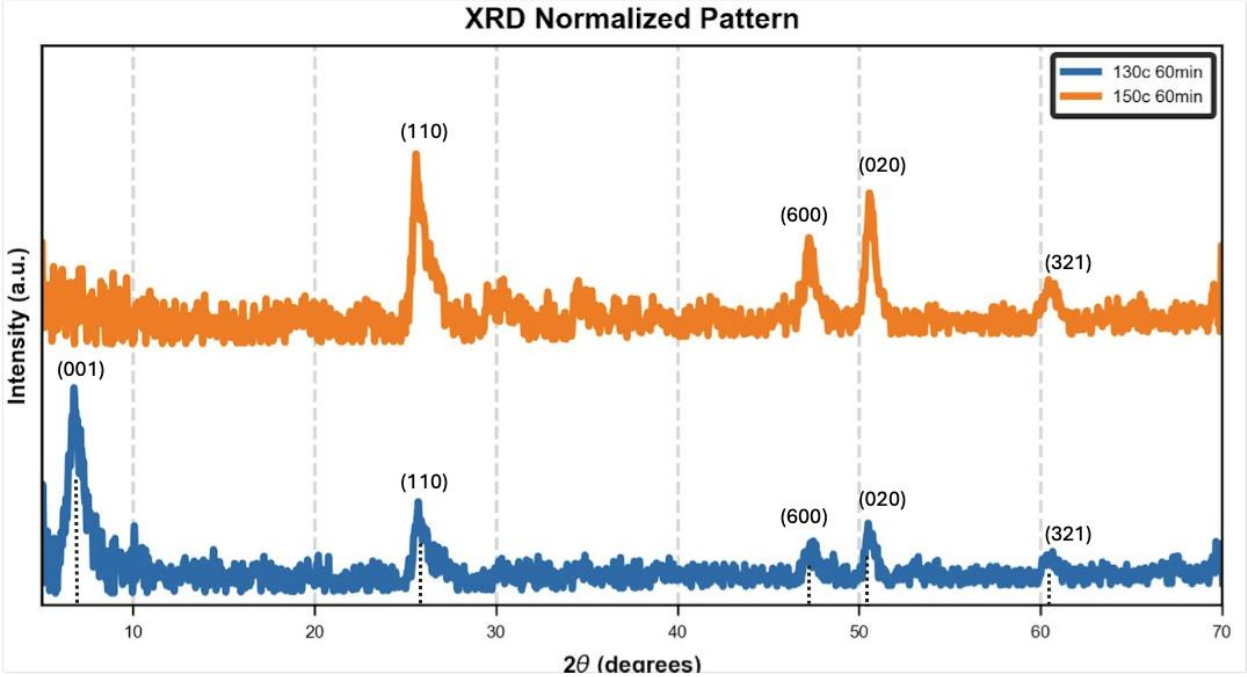

Figure 1: X-ray diffraction patterns of MWHT cathodes synthesized at 130°C, and 150°C. The lower synthesis temperature displays an intense low-angle (001) reflection at 2θ ≈ 7°, diagnostic of a strongly hydrated $V_2O_5 \cdot nH_2O$ whereas at 150°C this reflection is attenuated but retained while the (110), (600), (020), and (321) reflections sharpen. This trend confirms interlayer reorganization and improved crystalline ordering within the hydrated family.

3.1.2 Morphological Analysis and Microstructure (SEM)

The morphological evolution of MWHT synthesized V_2O_5 as a function of temperature was evaluated via scanning electron microscopy (SEM). At 130 °C, low-magnification SEM images show loosely packed, flower-like aggregates composed of thin, crumpled V_2O_5 nanosheets with abundant inter-particle voids from the sub-micrometer to tens-of-micrometer scale. Higher magnification reveals pronounced wrinkling, torn edges, and locally fibrillar textures along nanosheet surfaces. This open, defect-rich network is characteristic of early-stage growth in hydrothermal and microwave-assisted V_2O_5, where rapid supersaturation and anisotropic growth favor ultrathin flakes while restricting lateral thickening and surface smoothing [9].

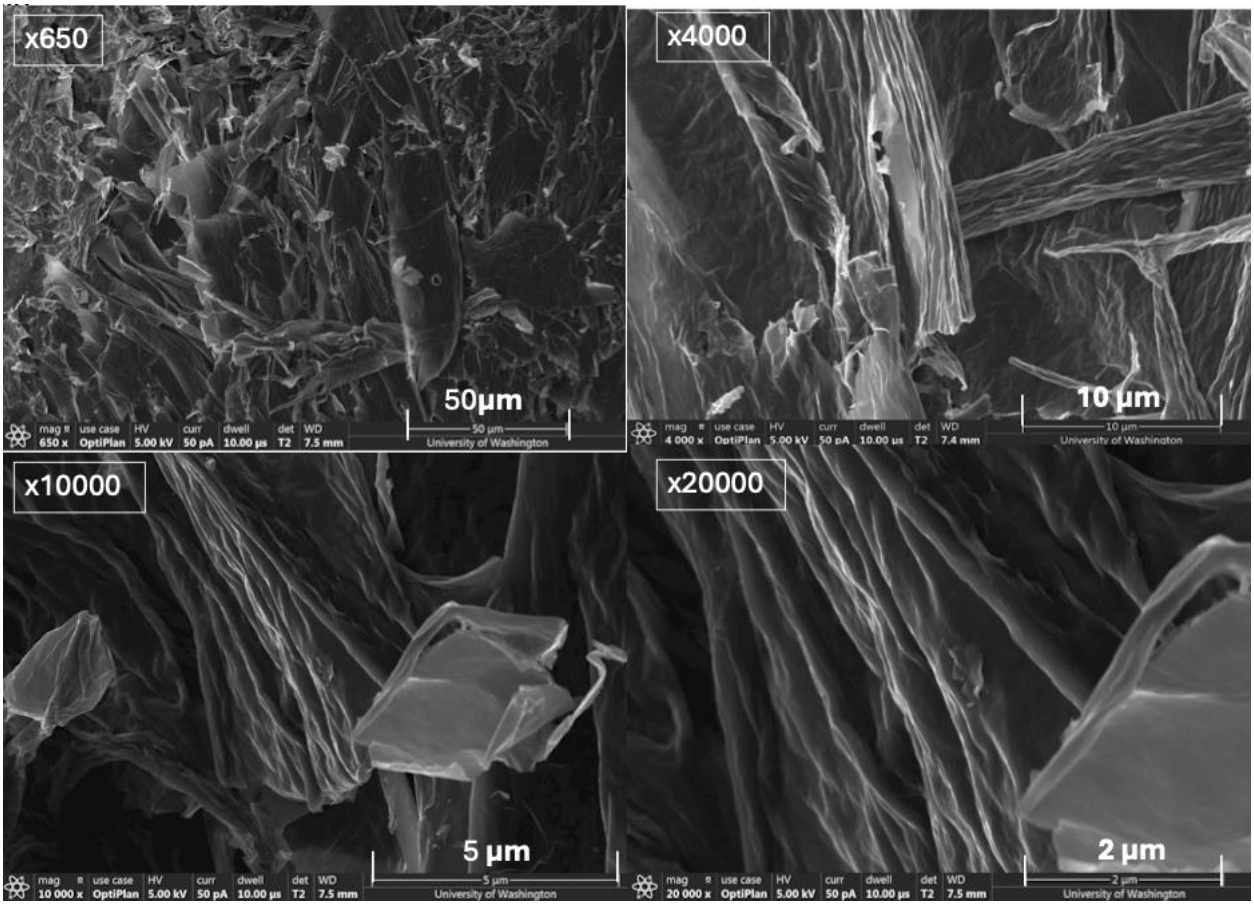

Figure 2*:* SEM micrographs of synthesized at varying magnifications for 130°C. The architecture comprises loosely packed, flower-like aggregates with extensive inter-particle voids. High-magnification imaging reveals crumpled nanosheets characterized by wrinkling and torn edges.

At 150 °C, low-magnification SEM images reveal compact, broad plate-like flakes assembled into dense lamellar domains with reduced inter-particle void space. The lateral dimension of individual sheets expands to several micrometers. At higher magnification, these flakes display planar basal surfaces and well-defined faceted edges. This 20 °C temperature increment drives a pronounced morphological transition, as elevated synthesis temperature accelerates solute diffusion and enhances surface attachment kinetics, promoting crystallite coarsening over continued nucleation [5].

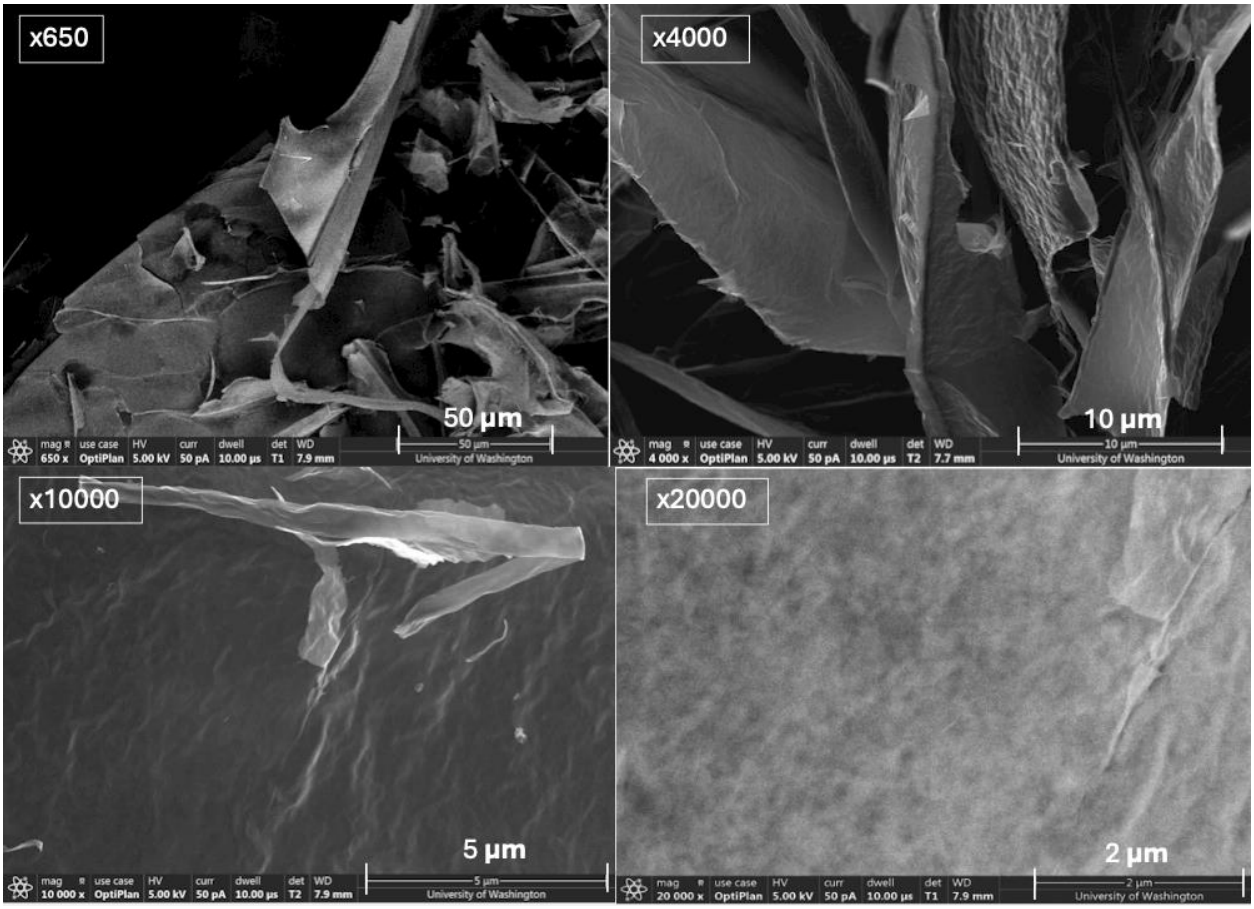

Figure 3: SEM micrographs of synthesized at varying magnifications for 150°C. The architecture exhibits a compact microstructure dominated by broad, plate-like flakes stacked into dense lamellar domains. High magnification imaging reveals smooth surfaces and straighter, faceted edges compared to the lower-temperature counterpart.

3.1.3 Elemental Composition (EDS)

Energy-dispersive X-ray spectroscopy (EDS) was performed to assess the bulk elemental composition of the cathodes (Figure 4). Both spectra detect vanadium (V) and oxygen (O) as the sole elements, confirming the absence of detectable secondary phases or contaminants [7]. The 150 °C sample yields an O:V atomic ratio close to 2:1 (O at 66.8%, V at 33.2%), consistent with a near-stoichiometric V_2O_5 bulk lattice. In contrast, the 130 °C sample exhibits a lower oxygen content (O: 36.4 at.%, V: 63.6 at.%), representing a significant deviation from the expected V_2O_5

stoichiometry. EDS has known limitations in quantifying light elements such as oxygen, and the observed deviation likely reflects the measurement artifacts rather than a true bulk stoichiometric difference. These results are treated as qualitative indicators of relative oxygen content only.

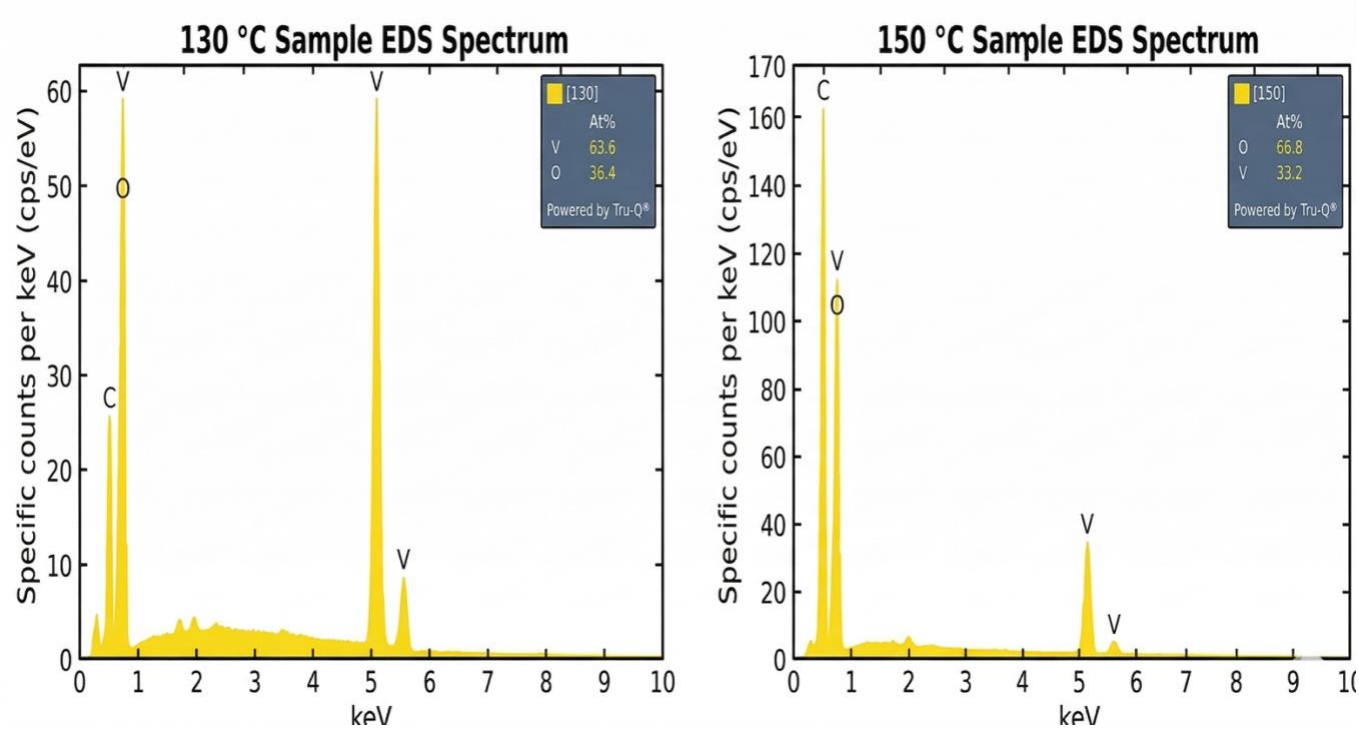

Figure 4: EDS spectra of V_2O_5 synthesize at 130 °C (left) and 150 °C (right) for 60 min. The 130 °C sample exhibits a non-stoichiometric, oxygen-deficient composition (63.6 at %V, 36.4 at% O). Increasing the synthesis temperature to 150 °C yields a near-stoichiometric O:V composition (33.2 at% V, 66.8 at% O). The carbon signal is an artifact originating from conductive sample substrate.

3.1.4 Local Structure (Raman Spectroscopy)

Raman spectroscopy was performed to probe the local structural order and vibrational characteristics of both MWHT samples (Figure 5). Both spectra display the characteristic fingerprint of the hydrated V_2O_5 framework, including the low-frequency skeletal mode at ~145 cm^{-1} and the high-frequency terminal vanadyl (V=O) stretching band at ~995 cm^{-1}, confirming the hydrated $V_2O_5 \cdot nH_2O$ phase established by XRD [9]. The 150 °C sample exhibits sharper, well-resolved peaks, a suppressed fluorescence background, and a narrower V=O stretching band, with increased relative intensity of the skeletal mode at approximately 145 cm^{-1} [9],[13]. The 130 °C sample, by contrast, displays an elevated fluorescence background attributable to surface organic residues or amorphous byproducts from incomplete crystallization [5], alongside inhomogeneous broadening of the vanadyl stretching band at approximately 995 cm^{-1}. This broadening reflects a distribution of local V=O bond lengths and angles, indicating reduced short-range structural order at 130 °C [5],[13]. The 20 °C thermal increment yields measurable improvement in local V=O bond homogeneity and reduced surface amorphous content in the 150°C sample.

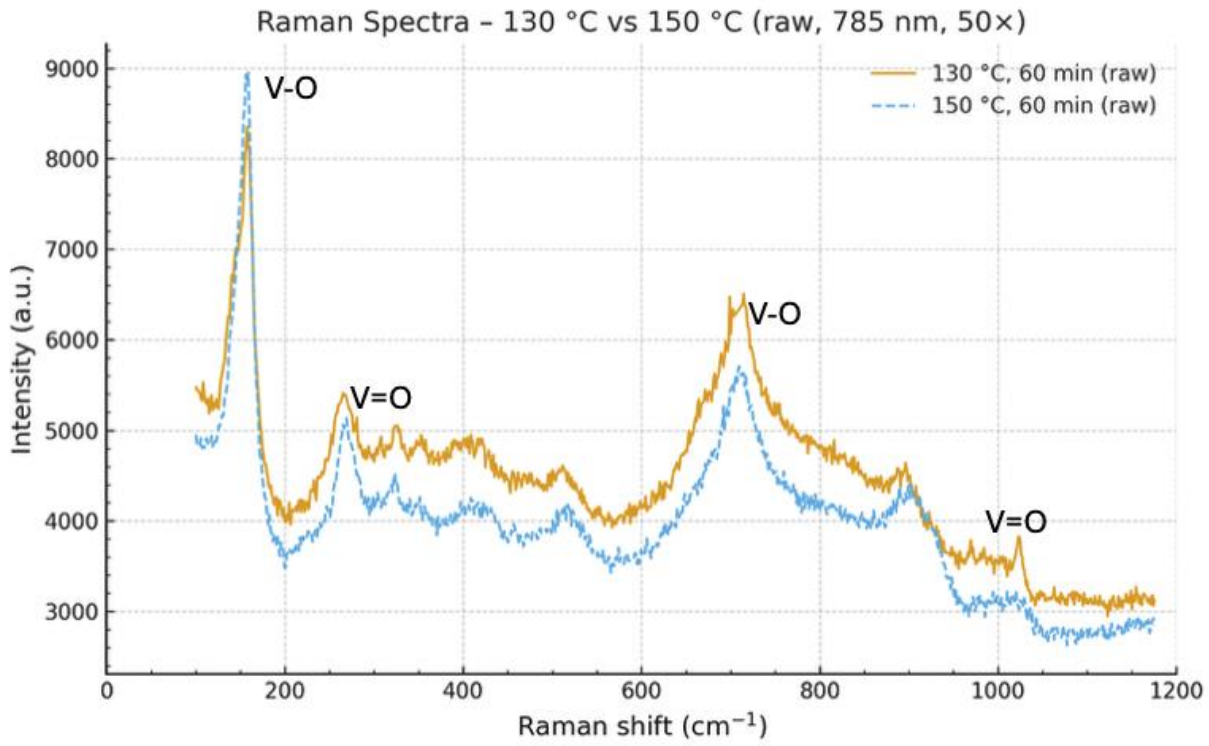

Figure 5: Raman spectra of MWHT synthesized at 130°C and 150°C. Characteristic peaks at ~145 cm^{-1} and ~995 cm^{-1} hydrated V_2O_5 phase. The 130°C sample exhibits elevated fluorescence and peak broadening, consistent with localize disorder. The 150°C sample displays suppressed background and sharper vibrational features, reflecting improved long-range atomic ordering.

3.1.5 Surface Chemistry (XPS)

High-resolution X-ray photoelectron spectroscopy (XPS) was performed to resolve the surface vanadium oxidation states and oxygen bonding environments (Figure 6). All spectra were calibrated using the adventitious C 1s peak at 285.0 eV. The V 2p core-level spectra were deconvoluted into two distinct spin-orbit doublets (V $2p_{3/2}$ and V $2p_{1/2}$) with a characteristic splitting (Δ) of ~7.4 eV, consistent with vanadium oxide frameworks [10]. The higher-binding-energy doublet (V $2p_{3/2}$ ≈ 518.0 eV; V $2p_{1/2}$ ≈ 525.4 eV) is assigned to V^{5+} centers, while the lower-energy pair (V $2p_{3/2}$ ≈ 516.7 eV; V $2p_{1/2}$ ≈ 524.1 eV) confirms coexisting V^{4+} species in both samples (Table 1). The V^{5+}/V^{4+} ratio increases from 6.5 to 8.8 with the 20 °C thermal

increment, indicating a greater degree of surface vanadium oxidation in the 150 °C cathode relative to the 130 °C cathode.

Table 1: XPS Surface Composition of Microwave-Hydrothermal V_2O_5 Cathodes.

Parameter	130°C – 60 min	150°C – 60 min
V^{5+} (% raw survey)[a]	26.9	28.0
V^{4+} (% raw survey)[a]	4.2	3.2
Total V (% raw survey)	31.1	31.2
V^{5+} (% normalized)[b]	86.6	89.8
V^{4+} (% normalized)[b]	13.4	10.2
V^{5+}/V^{4+} ratio	6.5	8.8
Lattice O^{2-} (530.8 eV, % raw)	54.0	54.0
Surface OH^- (531.7 eV, % raw)	10.7	10.7
Adsorbed H_2O (533.3 eV, % raw)	4.0	4.2

[a] Percentage of total XPS survey area (all elements).

[b] Normalized to total vanadium content (V^{4+} + V^{5+} = 100%).

To probe whether this V^{4+} excess originates from bulk oxygen loss or incomplete precursor oxidation, the O 1s spectra were examined. The O 1s spectra were deconvoluted into three

components: structural lattice oxygen (V–O, ~530.8 eV), surface hydroxyls (~531.7 eV), and adsorbed water (~533.3 eV) [10],[13]. The fractional areas remain consistent across both cathodes: lattice O^{2-} (54.0%), surface OH^- (10.7%), and adsorbed H_2O (4.0% vs. 4.2%), confirming that surface oxygen stoichiometry is preserved between synthesis conditions. The elevated V^{4+} concentration in the 130 °C cathode reflects incomplete precursor oxidation, where the lower thermal driving force was insufficient to fully convert V^{4+} centers to the V^{5+} state. These V^{4+} sites introduce local lattice distortions that impede Zn^{2+} transport within the host framework [13].

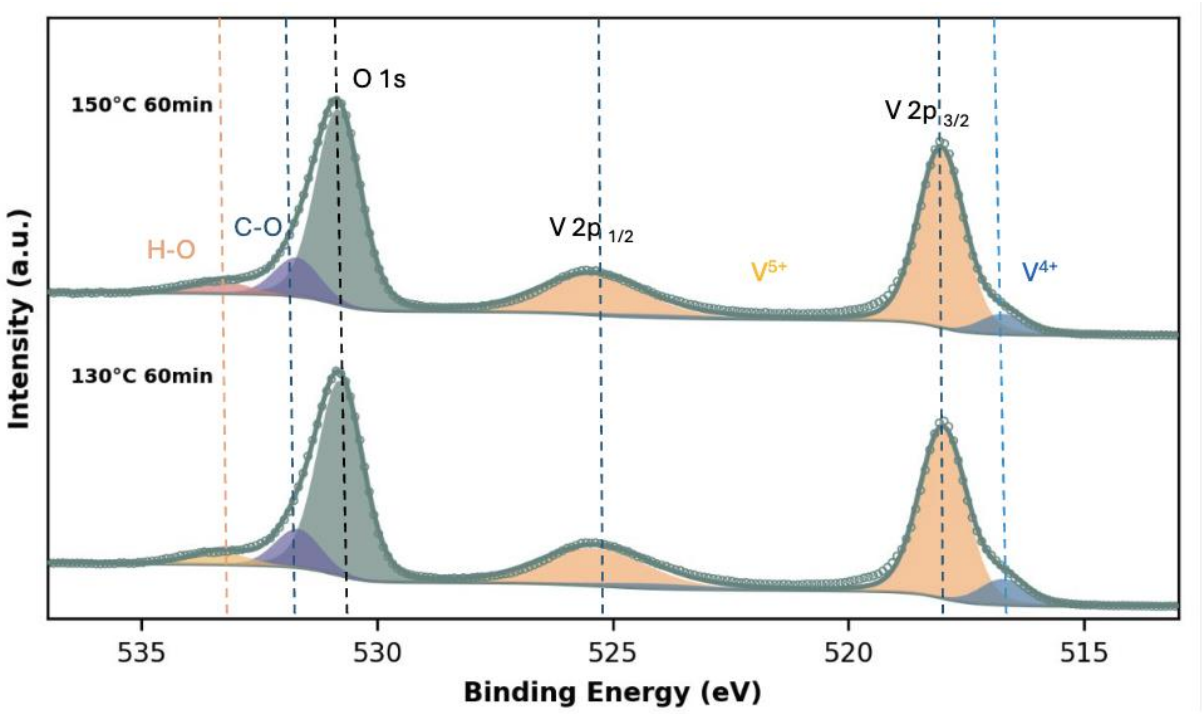

Figure 6: High-resolution V 2p and O 1s XPS spectra of the 130°C and 150°C cathodes. In the V 2p region, deconvolution of the V $2p_{3/2}$ envelope resolves two oxidation states: V^{5+} (≈ 518.0 eV) and V^{4+} (≈ 516.7 eV), with the V^{5+}/V^{4+} ratio increasing from 6.5 at 130°C to 8.8 at 150°C. In the O 1s region, three components are identified: lattice oxygen (≈ 530.8 eV), surface hydroxyls (≈ 531.7 eV), and adsorbed water (≈ 533.3 eV); their relative fractional areas remain unchanged between both cathodes, confirming preserved bulk oxygen stoichiometry across synthesis conditions.

3.2 Electrochemical Performance

The electrochemical performance of both cathodes was evaluated through rate capability testing and long-term cycling stability. The 20 °C synthesis temperature increment produces measurable differences in charge storage kinetics and capacity retention, as quantified by GCD measurements across 0.5 to 4 A g^{-1} (Figure 7) and extended cycling at 4 A g^{-1} over 3000 cycles (Figure 8).

3.2.1 Rate Capability (GCD)

Rate capability was assessed in CR2032 coin cells by incrementally stepping the current density from 0.5 to 1, 2, 3, and 4 A g^{-1}, with five consecutive cycles held at each rate within a potential window of 0.2–1.6 V vs. Zn^{2+}/Zn (Figure 7). Discharge capacities were normalized to the active V_2O_5 mass. The current density sequence was completed before returning to 0.5 A g^{-1} to confirm reversibility.

At 0.5 A g^{-1}, the 150 °C cathode delivers 330 mAh g^{-1}, compared with 290 mAh g^{-1} for the 130 °C sample. Both electrodes exhibit monotonic capacity decay with increasing current density. At 4 A g^{-1}, the 150 °C cathode retains 238 mAh g^{-1} (79% retention), while the 130 °C sample retains only 165 mAh g^{-1} (62% retention). Upon return to 0.5 A g^{-1}, both electrodes recover a measurable portion of their initial capacity, confirming that capacity decay is largely reversible. The 17 percentage-point retention gap between the two cathodes is attributed to the lower V^{4+} defect density and improved crystalline ordering of the 150 °C framework established in Section 3.1 [2].

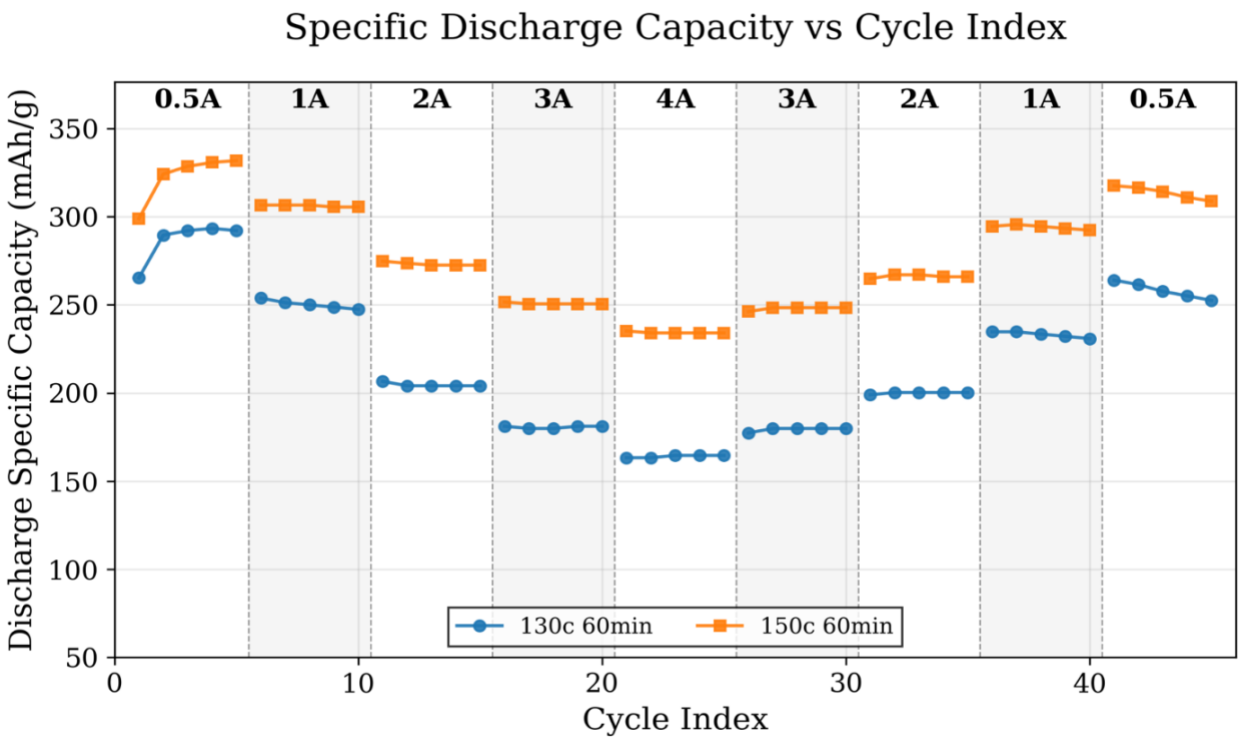

Figure 7: Rate performance of MWHT cathodes synthesized at 130°C and 150°C. Specific discharge capacity as a function of current density (0.5 to 4.0 mAh g^{-1}). The 150°C sample yields 330 mAh g^{-1} at 0.5 A g^{-1} and 79% retention (238 mAh g^{-1}) at 4.0 A g^{-1}, whereas the 130 °C cathode exhibits only 62% retention. Capacity recovery upon returning to 0.5 A g^{-1}, validates reversible intercalation kinetics for both frameworks.

3.2.2 Cycling Stability

Extended galvanostatic cycling over 3000 cycles at 4 A g^{-1} reveals distinct degradation behaviors for the two cathodes (Figure 8). At cycle onset, the 150°C sample delivers an initial capacity of 250 mAh g^{-1} compared to 190 mAh g^{-1} for the 130 °C sample. The 130 °C electrode exhibits a steeper capacity decay within the first 500 cycles before transitioning to a gradual decline, ending at 52.6% retention. The 150 °C electrode maintains a linear fading profile throughout the full 3000 cycles, retaining 64% of its initial capacity.

The accelerated early-cycle decay of the 130 °C cathode is attributed to its elevated V^{4+} defect density. These V^{4+} sites introduce charge-trapping defects that impede Zn^{2+} transport and are expected to generate local lattice distortions that further destabilize the host framework under repeated Zn^{2+} insertion and extraction [11],[13]. The better-ordered 150 °C cathode shows greater resistance to these failure modes, consistent with its higher V^{5+}/V^{4+} ratio and well-faceted lamellar morphology identified in Section 3.1. Its more ordered framework acts as a more stable host lattice under prolonged high-rate cycling conditions.

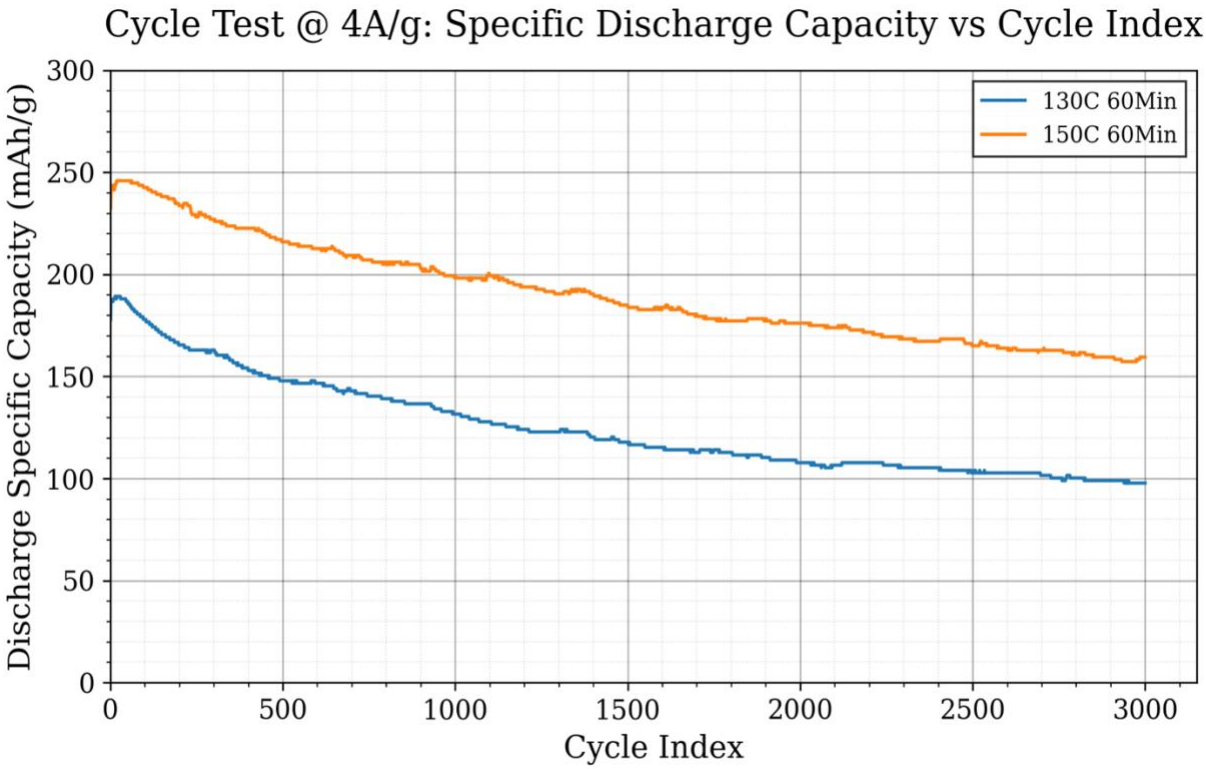

Figure 8: Long-term galvanostatic cycling of MWHT cathodes at 4 A g^{-1}. Comparison of specific discharge capacity over 3000 cycles for samples synthesized at 130°C and 150 °C. The 150 °C framework maintains 160 mAh g^{-1} (64% retention), significantly outperforming the disordered 130 °C phase (52.6% retention).

3.3 Kinetics and Interfacial Behavior

3.3.1 Charge Storage Mechanism (CV)

CV profiles were collected at 0.2 mV s^{-1} to evaluate the effect of synthesis temperature on redox reversibility and phase transition kinetics. Both electrodes exhibit the characteristic multi-step redox peaks of the $V_2O_5 \cdot nH_2O$ framework, with two anodic/cathodic couples from sequential V^{5+}/V^{4+} and V^{4+}/V^{3+} transitions during Zn^{2+} intercalation. Quantitative analysis of the peak parameters, summarized in Table 2, reveals the differences in peak separation and symmetry between the two synthesis conditions.

Table 2: Electrochemical parameters of $V_2O_5 \cdot$cathodes derived from CV (0.2 mv s^{-1})

Sample	Redox Couple	Anodic Potential (E_{ox}, V)	Cathodic Potential (E_{red}, V)	Peak Separation (ΔE_p, V)
130 °C	Pair 1 (V^{5+}/V^{4+})	1.10	0.90	0.20
130 °C	Pair 2 (V^{4+}/V^{3+})	0.69	0.50	0.19
150 °C	Pair 1 (V^{5+}/V^{4+})	1.08	0.89	0.19
150 °C	Pair 2 (V^{4+}/V^{3+})	0.70	0.51	0.19

The 130 °C electrode exhibits asymmetric peak behavior between the two redox regimes. The high-voltage V^{5+}/V^{4+} anodic peak (E_{ox} = 1.1 V) is sharp, while the low-voltage V^{4+}/V^{3+} feature (E_{ox} = 0.69 V) is broadened. This asymmetry is attributed to structural differences between surface and bulk redox environments where surface sites undergo facile redox while bulk sites

are kinetically hindered by the disordered, defect-rich lattice [2]. The elevated V^{4+} defect concentration in the 130 °C cathode introduces charge-trapping sites that raise the energetic barrier for Zn^{2+} extraction, producing voltage-dependent kinetic disparity between the two redox transitions [13]. The 150 °C electrode displays equivalent peak separations across both redox couples (ΔE_p = 0.19 V, Table 2), indicating uniform kinetic polarization at each redox transition and more complete multi-electron redox utilization relative to the kinetically asymmetric 130 °C cathode [2].

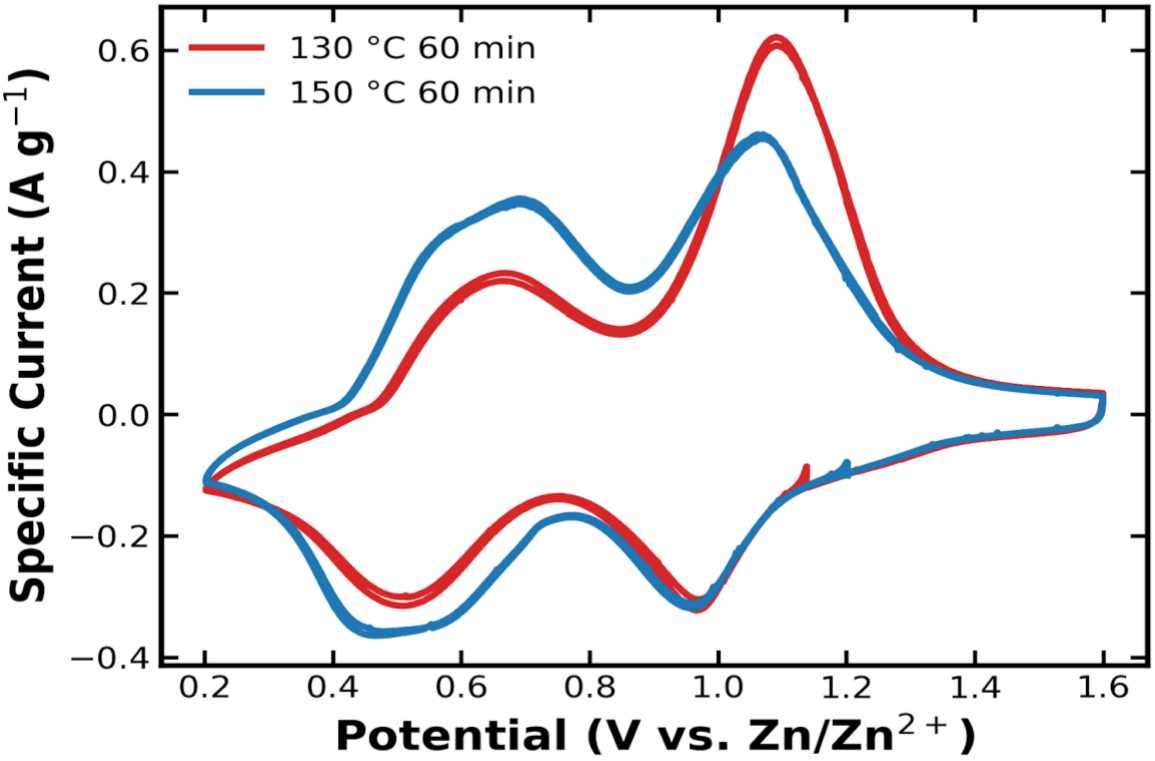

Figure 9: Cyclic Voltammetry (CV) profiles at 0.2 mV s^{-1} . Both electrodes exhibit characteristic multi-step redox signatures corresponding to sequential V^{5+}/V^{4+} and V^{4+}/V^{3+} transitions during intercalation. The 130 °C sample exhibits peak asymmetry, characterized by a broadened low-voltage anodic feature and variable peak separation. Conversely, the 150 °C sample yields symmetric redox profiles with equivalent peak separations ($\Delta E_p \approx 0.19$ V) across both couples.

3.3.2 Kinetic Analysis

CV measurements were performed at scan rates from 0.1 to 1.2 mV s^{-1} to evaluate rate-dependent charge storage kinetics. As shown in Figure 10, both samples exhibit redox pairs corresponding to multi-step Zn^{2+} intercalaction and sequential $V^{5+}/V^{4+}/V^{3+}$ transitions. The 130 °C sample exhibits pronounced peak broadening and increasing peak separation (ΔE_p) at higher scan rate, indicating growing kinetic polarization within the disordered framework. In contrast, the 150 °C sample maintains symmetric peaks and minimal ΔE_p across the full scan rate range, reflecting lower kinetic polarization and faster Zn^{2+} transport relative to the 130°C sample [2].

Quantitative kinetic analysis using the power-law relationship $i = av^b$ (see figure 11) shows a shift in the charge-storage mechanism. The 130 °C electrode yields b-values of 0.76 (anodic) and 0.64 (cathodic), indicative of mixed kinetics with a dominant diffusion-controlled component. The asymmetry between anodic and cathodic b-values further reflects the kinetic disparity between Zn^{2+} insertion and extraction in the defect-rich, disordered framework. The elevated V^{4+} defect concentration, tortuous diffusion pathways, and lattice strain associated with excess structural water collectively impede Zn^{2+} transport [11].

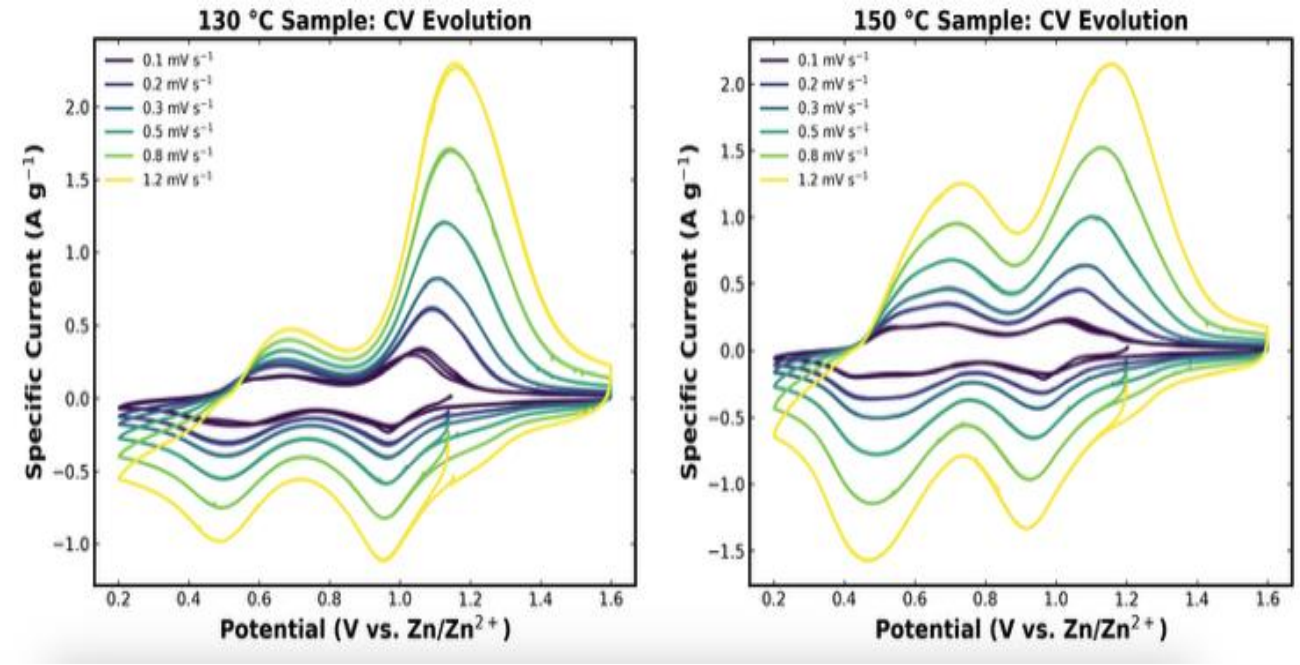

Figure 10: Scan rate dependent CV evolution (0.1 to 1.2 mv s^{-1}). The 130 °C sample exhibits pronounced peak broadening and increasing peak separation (ΔE_p) at elevated scan rates. The 150°C sample maintains symmetric peaks and minimal ΔE_p across the evaluated range.

The 150 °C electrode yields b-values of 0.88 (anodic) and 0.82 (cathodic), indicating pseudocapacitive-dominant charge storage [9]. In this regime, surface and near-surface redox sites dominate the charge storage response, shortening effective ion-transport distances and shifting the current-scan rate dependence toward capacitive behavior. The improved crystalline order of the 150 °C framework lowers the energetic barrier for Zn^{2+} transport and reduce charge-trapping at interfacial sites, accounting for the superior rate capability and cycling stability of the 150 °C cathode relative to the 130 °C cathode [13].

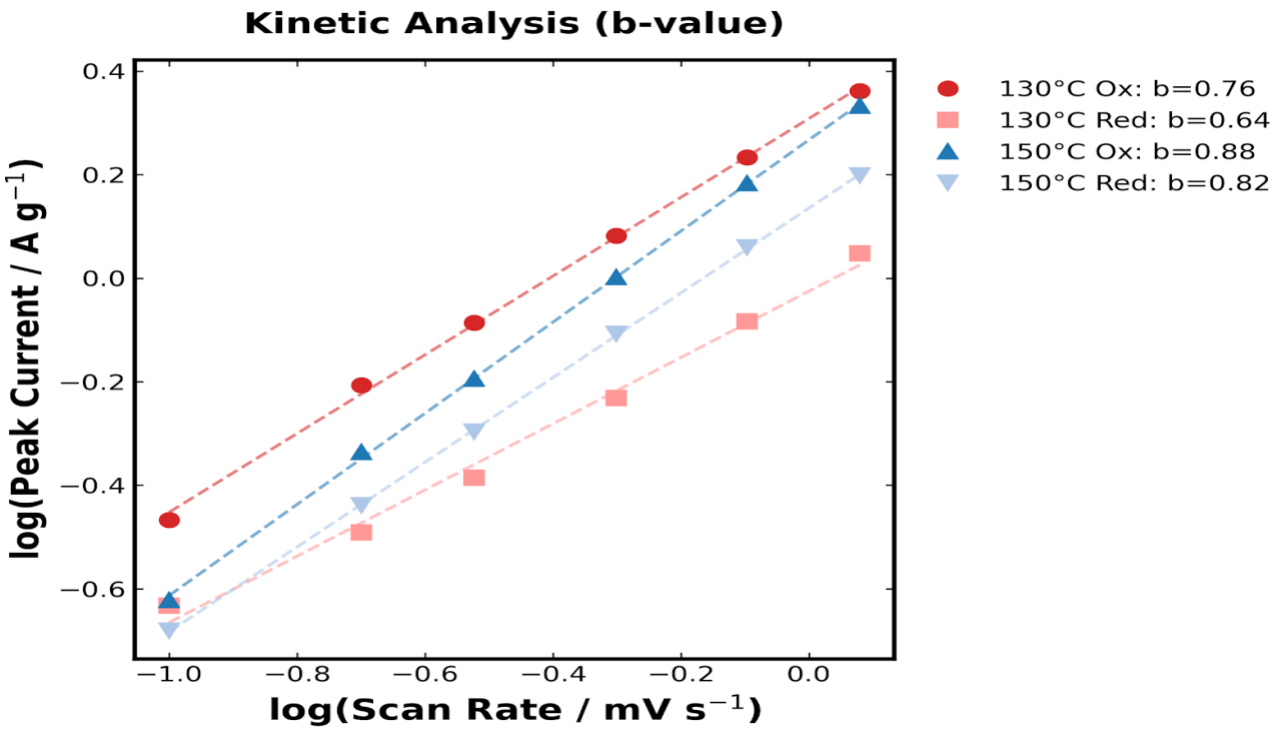

Figure 11: Power-law kinetic analysis. Log-log plots of peak current versus scan rate for 130 °C and 150°C samples. The 130 °C sample yields values of 0.76/0.64 (anodic/cathodic), confirming diffusion-limited kinetics[4]. Conversely, 150°C cathode displays b-values of 0.88/0.82, signifying a transition toward pseudocapacitance.

3.3.3 Charge transfer and interfacial resistance (EIS)

Electrochemical impedance spectroscopy was used to resolve interfacial charge-transfer resistance from solid-state Zn^{2+} diffusion kinetics. The Nyquist plots (Figure 12) exhibit a high-frequency semicircle attributed to charge-transfer resistance (Rct) at the cathode–electrolyte interface and a low-frequency Warburg tail (Zw) associated with solid-state Zn^{2+} diffusion within the host lattice [9]. Prior to CV activation, the 130°C cathode exhibits Rct ≈ 400 Ω whereas the 150°C cathode exhibits ≈ 320 Ω, representing a 20% reduction. The lower Rct of the 150°C sample is attributed to its denser lamellar morphology and reduced V^{4+} defect density (V^{5+}/V^{4+} =

8.8 versus 6.5), both of which are expected to reduce interfacial trapping and lower energetic barrier for Zn^{2+} insertion [11].

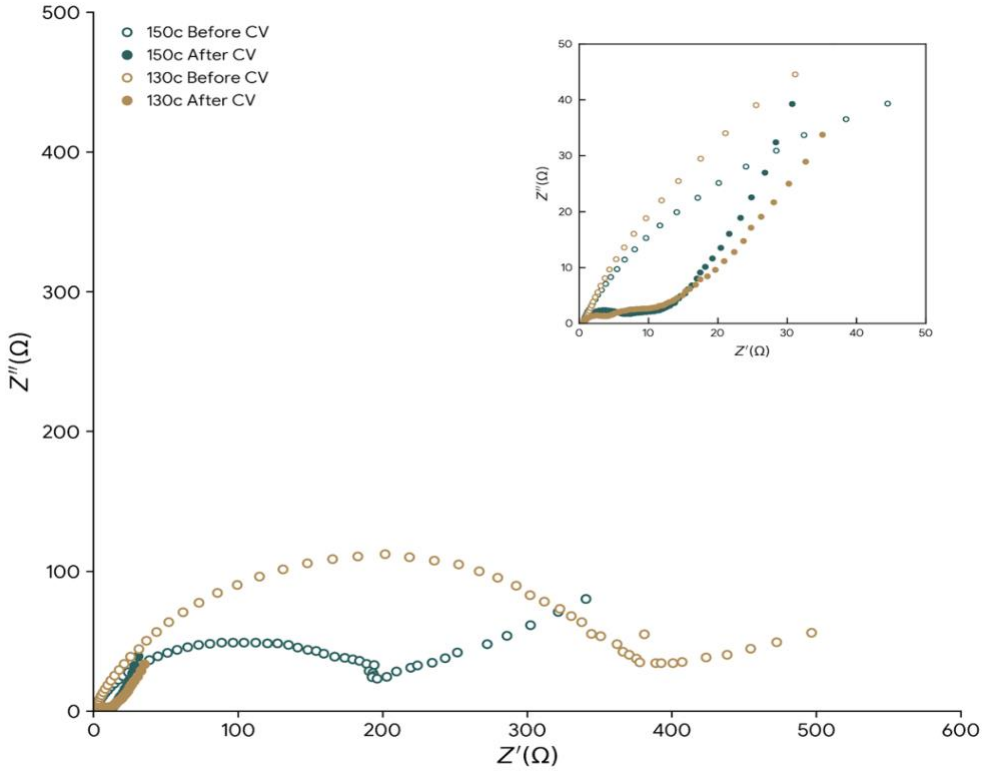

Figure 12: Nyquist plots of 130°C and 150°C cathodes before and after CV activation. Prior to activation, the 150°C cathode shows $R_{ct} \approx 320\ \Omega$ versus $\approx 400\ \Omega$ for the 130°C cathode. Following activation, R_{ct} drops to 10 – 20 Ω for both electrodes, attributed to improved electrolyte wetting and electrode conditioning. At low frequencies, the 150°C cathode displays a qualitatively steeper Warburg tail than the 130°C cathode, indicating lower solid-state Zn^{2+} diffusion resistance.

Following CV activation, both electrodes show Rct contraction to 10 Ω – 20 Ω, attributed to improved electrolyte wetting and electrode conditioning. In the low-frequency region, both samples exhibit diffusion-controlled tails. The 150 °C cathode's tail is qualitatively steeper and closer to the ideal 45° Warburg slope whereas the 130 °C electrode displays a flatter deviation at high Z′. The flatter tail of the 130 °C electrode indicates greater solid-state diffusion resistance,

consistent with its higher V^{4+} defect density and disordered nanosheet morphology [13]. Together with CV b-values reported in section 3.3.2, this EIS data supports the conclusion that 150 °C cathode exhibits lower charge-transfer and diffusion impedances than the 130 °C cathode.

4. Conclusions

This study establishes how a 20 °C increment in MWHT synthesis temperature governs defect density, crystalline ordering, and charge-storage kinetics in the hydrated $V_2O_5 \cdot nH_2O$ framework. The 130 °C cathode retains a strongly hydrated, disordered nanosheet morphology with a high V^{4+} defect concentration ($V^{5+}/V^{4+} = 6.5$). These V^{4+} sites introduce local lattice distortions that elevate and broaden Zn^{2+} deintercalation activation energies and impede ion transport rather than enhancing accessible redox capacity. The result is diffusion-dominant mixed kinetics (b = 0.76 anodic, 0.64 cathodic) and high charge-transfer resistance (Rct ≈ 400 Ω). Rate retention at 4 A g^{-1} is limited to 62%, and capacity decays to 52.6% after 3000 cycles. The accelerated decay within the first 500 cycles is attributed to vanadium dissolution and inactive byproduct formation reported for disordered, strongly hydrated vanadium oxide phases. The 150 °C cathode exhibits improved long-range crystalline order, a reduced V^{4+} defect density ($V^{5+}/V^{4+} = 8.8$), and well-faceted lamellar morphology. Charge storage shifts toward pseudocapacitive-dominant behavior (b = 0.88 anodic, 0.82 cathodic) with a 20% reduction in charge-transfer resistance (Rct ≈ 320 Ω). The cathode delivers 330 mAh g^{-1} at 0.5 A g^{-1}, 79% rate retention at 4 A g^{-1}, and 64% capacity retention over 3000 cycles at 4 A g^{-1}. These findings establish MWHT synthesis temperature as a readily accessible parameter for reducing charge-trapping defect density and improving structural ordering in hydrated vanadium oxide cathodes for AZIBs.

5. Future work

Future work should decouple bulk mass transport kinetics from interfacial degradation in the $V_2O_5 \cdot nH_2O$ framework. Galvanostatic intermittent titration technique (GITT) measurements will map potential-dependent Zn^{2+} diffusion coefficients (D_Zn) across the full intercalation window. HR-TEM and XPS depth profiling will resolve the chemical architecture and passivating function of the cathode–electrolyte interphase (CEI). Thermogravimetric analysis (TGA) is necessary to quantify structural water content in each hydrated phase, directly confirming the interlayer hydration difference between the 130 °C and 150 °C samples. The sharp structural divergence observed between 130 °C and 150 °C implies a narrow thermodynamic window. Investigation into dwell times (<60min) is necessary to map the crystallization onset and maximize microwave energy efficiency. Finally, the sluggish intrinsic electronic conductivity of the pristine $V_2O_5 \cdot nH_2O$ framework must be addressed. In-situ crystallization onto carbon scaffolds (e.g., rGO, CNTs) offers a route to improve electronic transport and stabilize the electrode architecture for prolonged high-rate cycling.

Acknowledgments

I would like to express my sincere gratitude to Professor Guozhong Cao and Xiaoxiao Jia for their invaluable support and guidance throughout this research. A portion of this work was conducted at the Molecular Analysis Facility (MAF), a National Nanotechnology Coordinated Infrastructure site at the University of Washington with technical support from MAF staff.

Conflict of Interest

There are no conflicts to declare.

References

[1] K. Zhu and W. Yang, “Vanadium-Based Cathodes for Aqueous Zinc-Ion Batteries: Mechanisms, Challenges, and Strategies,” *Acc. Chem. Res.*, vol. 57, no. 19, pp. 2887–2900, Oct. 2024, doi: 10.1021/acs.accounts.4c00484.

[2] A. Guo *et al.*, “A Comprehensive Review of the Mechanism and Modification Strategies of V_2 O_5 Cathodes for Aqueous Zinc-Ion Batteries,” *ACS Nano*, vol. 18, no. 40, pp. 27261–27286, Oct. 2024, doi: 10.1021/acsnano.4c09899.

[3] T. Wu, K. Zhu, C. Qin, and K. Huang, “Unraveling the role of structural water in bilayer V_2 O_5 during Zn^{2+} -intercalation: insights from DFT calculations,” *J. Mater. Chem. A*, vol. 7, no. 10, pp. 5612–5620, 2019, doi: 10.1039/C8TA12014E.

[4] S. Sariyer, N. M. Keppetipola, O. Sel, and R. Demir-Cakan, “Microwave-Assisted Rapid Hydrothermal Synthesis of Vanadium-Based Cathode: Unravelling Charge Storage Mechanisms in Aqueous Zinc-Ion Batteries,” *ChemSusChem*, vol. 18, no. 10, p. e202402445, May 2025, doi: 10.1002/cssc.202402445.

[5] M. A. Jalil *et al.*, “Impact of reaction temperatures on the particle size of V2O5 synthesized by facile hydrothermal technique and photocatalytic efficacy in dye degradation,” *AIP Adv.*, vol. 13, no. 1, p. 015010, Jan. 2023, doi: 10.1063/5.0125200.

[6] X. Jia, C. Liu, Z. Wang, D. Huang, and G. Cao, “Weakly Polarized Organic Cation-Modified Hydrated Vanadium Oxides for High-Energy Efficiency Aqueous Zinc-Ion Batteries,” *Nano-Micro Lett.*, vol. 16, no. 1, p. 129, Dec. 2024, doi: 10.1007/s40820-024-01339-y.

[7] X. Liu *et al.*, “Facile hydrothermal synthesis of V2O5 nanofibers as cathode material for aqueous zinc-ion batteries,” *J. Alloys Compd.*, vol. 896, p. 163071, Mar. 2022, doi: 10.1016/j.jallcom.2021.163071.

[8] X. Jia *et al.*, “Solvothermal Guided V2O5 Microspherical Nanoparticles Constructing High-Performance Aqueous Zinc-Ion Batteries,” *Materials*, vol. 17, no. 7, p. 1660, Apr. 2024, doi: 10.3390/ma17071660.

[9] K. Guo *et al.*, “Facile and Rapid Synthesis of Porous Hydrated V2O5 Nanoflakes for High-Performance Zinc Ion Battery Applications,” *Nanomaterials*, vol. 12, no. 14, p. 2400, Jul. 2022, doi: 10.3390/nano12142400.

[10] G. Silversmit, D. Depla, H. Poelman, G. B. Marin, and R. De Gryse, “Determination of the V2p XPS binding energies for different vanadium oxidation states (V5+ to V0+),” *J. Electron Spectrosc. Relat. Phenom.*, vol. 135, no. 2–3, pp. 167–175, Apr. 2004, doi: 10.1016/j.elspec.2004.03.004.

[11] Z. Xing *et al.*, “Facing the capacity fading of vanadium-based zinc-ion batteries,” *Trends Chem.*, vol. 5, no. 5, pp. 380–392, May 2023, doi: 10.1016/j.trechm.2023.02.008.

[12] P. R. Reshma, C. Lakshmanan, A. K. Prasad, and S. Dhara, “High performance bilayer 2D V2O5 cathode for Zn-ion and Zn/Li hybrid metal-ion intercalation battery,” *Sci. Rep.*, vol. 15, no. 1, p. 31543, Aug. 2025, doi: 10.1038/s41598-025-17294-6.

[13] T. Selvam, D. Dhinasekaran, B. Subramanian, and A. R. Rajendran, “Dual ion insertion and oxygen vacancy engineering in nanostructured V2O5 cathodes for enhanced Zn-ion battery performance and stability,” *J. Power Sources*, vol. 636, p. 236593, Apr. 2025, doi: 10.1016/j.jpowsour.2025.236593.